American Mineralogist, Volume 88, pages 978–985, 2003

Dissolution of strontianite at high *P-T* conditions: An in-situ synchrotron X-ray fluorescence study

CARMEN SANCHEZ-VALLE,[1,*] ISABELLE MARTINEZ,[2] ISABELLE DANIEL,[1] PASCAL PHILIPPOT,[3] SYLVAIN BOHIC,[4] AND ALEXANDRE SIMIONOVICI[4]

[1]Laboratoire de Sciences de la Terre, UMR 5570 CNRS-ENS Lyon-UCB Lyon 1, 46, Allée d'Italie, F-69364 Lyon Cedex 07, France
[2]Laboratoire de Géochimie des Isotopes Stables, Tour 54-64, IPGP Paris VII 2, place Jussieu, 75251 Paris Cedex 05, France
[3]Laboratoire de Geosciences Marines, CNRS-IPGP, case 89, Paris VI-VII 4, place Jussieu, 75005 Paris, France
[4]ID22, European Synchrotron Radiaction Facility 6, rue Jules Horowitz, BP 220, F-38043 Grenoble Cedex, France

ABSTRACT

In-situ measurements of the amount of dissolution of carbonate minerals at high pressures (up to 3.6 GPa) and temperatures (up to 523 K) are reported. Using an externally heated diamond anvil cell (DAC) and synchrotron X-ray fluorescence (SXRF), the extent of dissolution of strontianite ($SrCO_3$) has been followed as a function of time by monitoring the fluorescence of Sr cations in the fluid surrounding the crystal. This work demonstrates that Sr^{2+} concentrations as low as 1000 ppm can be detected and measured in-situ in a DAC, using a forward transmission geometry. The preliminary data presented here indicate that this technique has high potential for determining solution composition in high-pressure and high-temperature geochemical studies.

INTRODUCTION

Altered oceanic crust undergoes devolatilization as it is subducted. Fluids released into the mantle consist of CO_2-bearing aqueous solutions containing other dissolved components, especially alkali, alkaline-earth halides and carbonates, as inferred from fluid-inclusion studies (Roedder 1984). These fluid phases then react with mantle minerals leading to mantle wedge metasomatism. Therefore, estimation of mantle metasomatism requires knowledge of minerals solubilities in fluids over a broad range of pressure-temperature conditions. Furthermore, an accurate knowledge of solution equilibria and solubilities is required to interpret kinetic studies of mineral dissolution and precipitation. Despite the recognized importance of fluids expelled from subducted slabs as metamorphic agents (e.g., Peacock 1990; Scambelluri and Philippot 2000), their chemical composition and reactivity toward mantle minerals are known from high-pressure studies carried out in quenched samples (Ayers and Eggler 1995; Brenan et al. 1995; Keppler 1996; Ayers et al. 1997; Stalder et al. 1998; Newton and Manning 2000a, 2000b; Melzer and Wunder 2001).

Because CO_2 is a major volatile component in deep fluids, the dissolution of carbonate minerals plays an important role in controlling the composition and properties of those fluids. Unfortunately, very few solubility studies have been carried out on carbonates at elevated P and T and most of these are dedicated to calcite (Sharp and Kennedy 1965; Fein and Walther 1987). Fein and Walther (1987) measured calcite solubility in H_2O-CO_2 fluids to 620 °C and 2 kbar pressure, and showed that, at constant mol fraction of CO_2, calcite solubility increases as a function of pressure, but decreases with increasing temperature.

Strontianite ($SrCO_3$) has been chosen in this study instead of calcite for the following reasons: (1) its solubility, although different from that of aragonite and calcite by almost one order of magnitude, follows the general behavior observed for calcium carbonates with *P-T* for the limited investigated range (Plummer and Busenberg 1982; Busenberg et al. 1984; Fein and Walther 1987); (2) Sr is amenable to solubility measurement through in-situ X-rays fluorescence whereas Ca is not; (3) Sr is a widely used geochemical tracer of hydrothermal processes (McCulloch et al. 1991; Hawkesworth et al. 1993); and (4) modeling its behavior in natural Ca-rich solid solutions requires data on its own end-member (Plummer and Busenberg 1987).

Early studies of $SrCO_3$ solubility were performed in pure water, at various CO_2 partial pressures and temperatures. For instance, Haehnel (1924) measured the solubility of strontianite at 18 °C and P_{CO_2} of 1.0 atm, McCoy and Smith (1911) investigated CO_2 partial pressures in the range 0.05–1.1 atm range and 25 °C. Helz and Holland (1965) reported measurements of strontianite solubility at 50, 100, and 200 °C under CO_2-pressures between 1.0 and 50.0 atm. More recently, Millero et al. (1984) measured the solubility of $SrCO_3$ in 0.1 to 6 *m* NaCl solutions at 25 °C. Finally, Busenberg et al. (1984) reported solubility data in CO_2-H_2O solutions between 2 and 91 °C, by measuring quenched fluids by EDTA titration. All these studies have shown that the solubility of strontianite decreases with increasing temperature at constant CO_2 pressures, as is the case for other alkaline earth carbonates at subcritical conditions (Plummer and Busenberg 1982).

Although the solubility constant of strontianite (*K*s) is well documented in the 2–200 °C temperature range (Helz and Holland 1965; Busenberg et al. 1984), the behavior of the $SrCO_3$-

* E-mail: Carmen.Sanchez@ens-lyon.fr

0003-004X/03/0007–978$05.00

H_2O system at high pressure is poorly known. A single high-pressure study by Helz and Holland (1965) showed that $SrCO_3$ solubility increased with increasing total pressure from 1 to 50 atm. This behavior observed at moderate pressure cannot be extrapolated reasonably to the pressures relevant to the upper mantle. Direct measurements at upper mantle pressures are thus required.

High-pressure, high-temperature mineral solubilities usually have been measured using weight-loss methods (Manning 1994) and by analyzing the resulting quenched fluids and solids (Walther and Orville 1983; Manning and Boettcher 1994; Keppler 1996; Aranovich and Newton 1999), but collecting kinetic data in these rapidly quenched small samples is a tedious task. Therefore, it is of great importance to measure in-situ mineral dissolution rates at simultaneous high *P-T* conditions. Recently, Zotov and Keppler (2002) utilized in-situ Raman spectroscopy to measure the dissolution of silica at high *P* and *T* (1.4 GPa, 900 °C) and the speciation of silicate species in the fluid. Due to its high detection limit, Raman spectroscopy only can be used in highly soluble minerals. For instance, we calculated the detection limits for carbonates species in aqueous solution to be 0.2 *m* (Martinez 2002, personal communication).

Synchrotron X-ray fluorescence spectroscopy (SXRF), used for fluid-inclusion characterisation (Frantz et al. 1988; Mavrogenes et al. 1995; Philippot et al. 1998; Ménez et al. 2001, 2002), is a powerful technique for determining trace-element distribution and concentration with micrometer resolution and ppm sensitivity. Progress in synchrotron light sources have improved the sensitivity of this method, so that quantification of element concentration from a sample placed between the two diamond windows of a diamond anvil cell (DAC) is now possible. In-situ X-ray fluorescence measurements in a DAC are possible on second-generation synchrotron sources by using specially designed diamond-cells and optimized geometries (Schmidt and Rickers 2002). As shown in the present study, third-generation synchrotrons allow the use of a forward-transmission geometry without modifying the original design of the DAC, thus achieving higher-pressure conditions.

In this work, we report in-situ experiments on the dissolution of carbonate minerals at pressures up to 3.6 GPa and temperatures up to 523 K, relevant to cold subducting slabs. The dissolution of a strontianite ($SrCO_3$) crystal in aqueous solution has been followed in an externally heated DAC by monitoring the fluorescence of Sr^{2+} cations in the fluid as a function of *P-T* conditions. The crystal was placed in a $RbNO_3$ solution (0.01 *m* at ambient conditions) to follow the evolution of the Sr/Rb ratio in the fluid, this ratio being more accurately measured than absolute Sr concentrations. Indeed, the imprecision of correction procedures cancel out in the case of two elements with close energies for emitted X-rays (14.2 keV and 13.4 keV for Sr and Rb, respectively). To use the $K\alpha$ intensities ratio as a tracer of the dissolution process, solutions with known concentrations of Rb and Sr were used to calibrate their fluorescence yields in the same experimental configuration, i.e., loaded in the DAC.

The aim of the present study was to demonstrate the feasibility of in-situ measurements of mineral dissolution rates at upper mantle *P-T* conditions. We focus in this paper on the technical aspects and experimental details of this work. Dissolution of strontianite is examined up to 3.6 GPa and 523 K and the effect of pressure briefly discussed. These results will allow further thermodynamic and kinetic modelling of carbonate dissolution in deep fluids.

EXPERIMENTAL METHODS

Starting materials

Freshly prepared aqueous solutions of strontium nitrate [$Sr(NO_3)_2$] and rubidium nitrate ($RbNO_3$), 0.1 *m* at ambient conditions, were used to prepare standard solutions of known concentrations of these elements (Sr = 0.02 *m*-Rb = 0.08 *m*, Sr = 0.05 *m*-Rb = 0.05 *m*, Sr = 0.08 *m*-Rb = 0.02 *m*, and Sr-Rb = 0.001 *m*). The compositions of the five solutions were measured after preparation by analysis of Rb and Sr concentrations using flame or flameless atomic absorption spectrometry.

Fragments of a natural single crystal of strontianite were used throughout this work. The composition of a known weight of $SrCO_3$ dissolved in diluted HNO_3 was analysed by Inductively Coupled Plasma Mass Spectrometry (ICP-MS) and Inductively Coupled Plasma Atomic Emission Spectrometry (ICP-AES) for Ba and Ca, respectively. Barium was found to be present in trace amounts only (60 ± 3 ppm) whereas the concentration of Ca was much higher (16 000 ± 160 ppm).

Diamond-anvil cell techniques

All experiments were performed in a membrane-type DAC (Chervin et al. 1995) equipped with an external resistive Watlow heater surrounding the body of the cell. In this device, pressure is generated by flushing He gas into the membrane chamber. The induced membrane deformation drives the movement of the DAC piston. Low-fluorescence, type Ia diamonds with 500 µm culets were used. Pressure chambers were formed from 300 µm diameter holes drilled in a rhenium gasket preindented at about 60 µm thickness.

For fluorescence calibrations, the standard solutions were loaded into the cooled cell under a binocular microscope without transmitted light to avoid evaporation. Pressure inside the compression chamber was calculated from the calibrated shift of the R_1 fluorescence line of a 5 µm ruby chip (Cr^{3+}: 3000 ppm) also loaded into the experimental volume (Mao et al. 1978). Errors in pressure are estimated to be 5% of the pressure values. Ruby fluorescence was excited and collected using a portable optical system (PRL) installed for this purpose on the beamline. This device consists of a laser diode (532 nm wavelength) for fluorescence excitation, and of a spectrometer (600 grooves/mm) for fluorescence analysis; it was mounted on a motorized stage, which allowed it to move away from the X-ray path after each pressure measurement (Fig. 1).

For solubility experiments at high pressure and temperature, the cell was loaded with a single crystal of strontianite (~30 × 20 × 20 µm) together with a ruby chip, and subsequently filled with the 0.01 *m* $RbNO_3$ aqueous solution (Fig. 2). Temperature was read with a K-thermocouple, calibrated before experiments, and included in the heating device. Estimated uncertainties in temperature are ±2 K. Pressure was calculated from the calibrated shift of the R_1 fluorescence line of the ruby, after temperature correction (Ragan et al. 1992).

Synchrotron X-ray fluorescence (SXRF) at the ESRF ID22 beamline

Experiments were carried out at the ESRF undulator beamline µFID22, where a DAC was installed for the first time (Fig. 1). A focused 18 keV monochromatic incident beam, tuned by a double crystal fixed-exit silicon monochromator, was used for exciting the Sr$K\alpha$ (14.2 keV) and Rb$K\alpha$ (13.4 keV) fluorescence lines in the sample. The transmittance of one diamond anvil (2 mm thickness) for Sr$K\alpha$ and Rb$K\alpha$ fluorescence energies is 64% and 50%, respectively.

The focusing device consisted of a set of 56 parabolic Al Compound Refractive Lenses (CRL) (Snigirev et al. 1996; Lengeler et al. 1999); the CRL device delivers a beam intensity of approximately 2×10^9 photons/s with a spot-size of about 2×15 mm^2 on the sample. A PIN diode detector, operating in the current integration mode, was positioned before the sample to monitor the flux of the incident focused beam. The DAC was positioned in the image plane with a high-precision XYZθ remote-controlled stage, and aligned along the X-ray path. Secondary X-rays were collected at the rear-side of the cell with a Si(Li) solid-state diode detector (Eurisys Mesures, France) of 150 eV resolution at 5.89 keV, set at 15° from the incident beam in the horizontal plane (Fig. 1). The detector, placed 3 cm away from the cell, was mounted on motorized translation

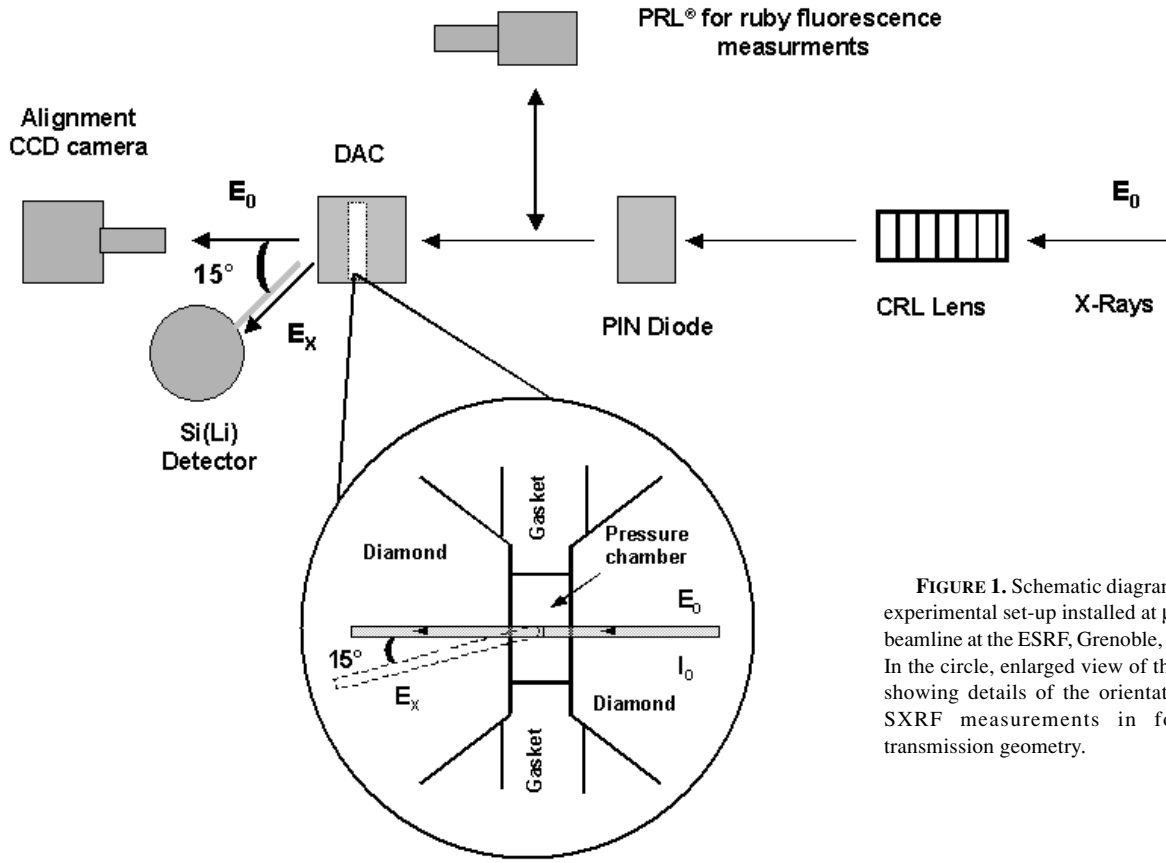

FIGURE 1. Schematic diagram of the experimental set-up installed at μFID22 beamline at the ESRF, Grenoble, France. In the circle, enlarged view of the DAC showing details of the orientation for SXRF measurements in forward transmission geometry.

stages and shielded with a collimator (ϕ = 4 mm) to reduce the contribution to the signal from Compton-scattered X-rays and thereby improve the fluorescence/scattering ratio. Under these conditions, the active area of the detector and the subtended solid angle are 12.5 mm^2 and 1.4×10^{-2} steradians, respectively. A high-resolution X-ray CCD camera (Princeton Scientific Instruments, USA), set behind the cell in transmission geometry, was used to align the sample with respect to the beam. Images were collected based on phase/absorption contrast, permitting the beam to be positioned in the sample with a precision of a few micrometers.

DATA COLLECTION AND ANALYSIS

To check for the absence of contribution to the Sr signal from the strontianite sample when the X-ray beam is focused in the fluid, a spectrum was recorded in the presence of the strontianite crystal before filling the cell chamber with the solution (background in Fig. 3). It does not display any significant Sr contribution from the crystal and allows the contribution to the background from Compton scattering off of the diamond anvils to be retrieved.

Fluorescence data were collected in two experimental runs by focusing the X-ray beam at a fixed point in the fluid and by following the increasing ratio of Sr and Rb $K\alpha$ peak areas as a function of *P-T* conditions. Fluorescence of the fluid was recorded with an exposure time of 1000 seconds and homogeneity of the solution was checked by analyzing different locations in the fluid.

Data analysis was performed using the WinAxil Software package (Vekemans et al. 1994) to obtain the area under the X-

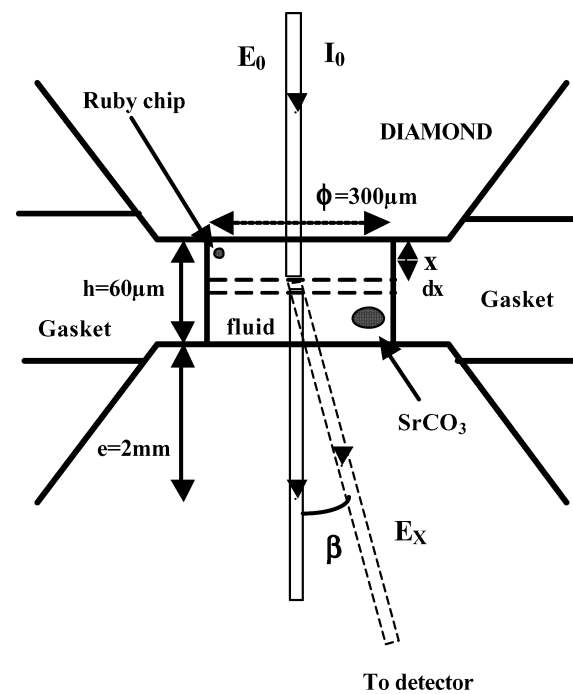

FIGURE 2. Schematic geometry used for correcting absorption in X-ray fluorescence measurements (Eq. 1). Note the path length through the diamonds and sample of the incoming beam (E_0) and the outgoing X-rays (E_X).

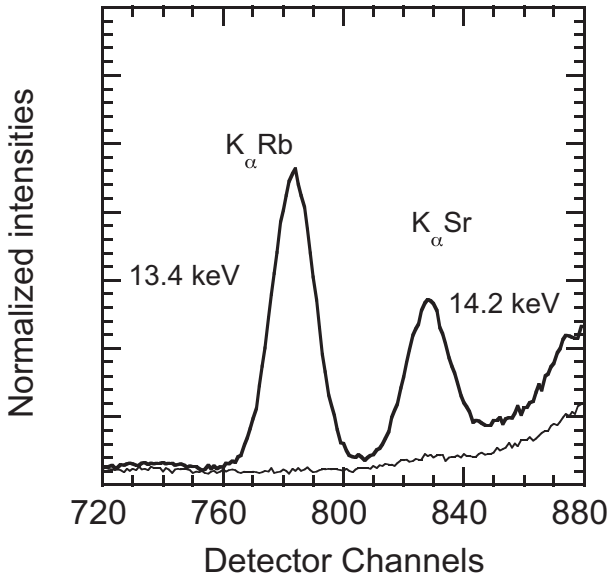

FIGURE 3. X-ray fluorescence spectrum collected in 300 seconds at 298 K and 0.1 GPa in a Sr-Rb 0.001 *m* aqueous solution (bold solid line). Spectrum recorded in the fluid-free cell, providing the contribution of diamond to the background (solid line).

ray lines, which is proportional to the concentration, and to correct for the X-ray photon background, arising from elastic (Rayleigh) and inelastic (Compton) scattering, arising mostly from diamonds in our experiments.

In addition, X-ray lines were analyzed in an alternative way using a standard curve-fitting routine (Peakfit). The experimental background recorded in the empty cell (Fig. 3) was subtracted from the spectra and the Rb and Sr fluorescence peaks fitted to a Voigt shape. The good agreement between peak areas, and thus between the number of photons determined by both methods, verifies the assumption that the aqueous solution contributes only slightly to the background.

Corrections accounting for X-ray attenuation in the different parts of the pathway to the detector were performed according to the protocol proposed in Philippot et al. (1998), modified to our specific experimental configuration. The geometry of beam-sample interaction is represented in Figure 2. For a monochromatic incident beam, the number of photons $N(E_X, Z_i)$ corresponding to the E_X line of an element Z_i arriving at the detector in a counting time t is:

$$N(E_X,Z_i) = N_0 t \frac{\Omega}{4\pi}\varepsilon(E_X)\exp\left[-\left(\mu_{E_0}^{\text{diam}} + \frac{\mu_{E_X}^{\text{diam}}}{\cos\beta}\right)e\rho_{diam}\right]\exp\left[-\frac{\mu_{E_X}^{air}\rho_{air}l}{\cos\beta}\right]$$
$$C_i\sigma_F(E_0,Z_i)\rho_{\text{fluid}}\int_0^h \exp\left[-\left(\mu_{E_0}^{\text{fluid}} + \frac{\mu_{E_X}^{\text{fluid}}}{\cos\beta}\right)\rho_{\text{fluid}}X\right]dX \quad (1)$$

with N_0 being the number of incident photons per unit time (ph/s) with an energy E_0, and μ_j^a are the mass-absorption coefficients (cm^2/g) of the crossed material a (diamonds, fluid, or air) at the energy j (incident E_0 or fluorescence E_x beam). Considering that the crossed material a is composed of n elements, μ_j^a becomes:

$$\mu_j^a = \sum_{i=1}^{n} Ci\mu(Z_i) \quad (2)$$

with $\mu_{(Zi)}$ representing the mass absorption coefficient of the element Z_i, and C_i its concentration in the material (in $g_{Zi}/g_{\text{material}}$). The mass-absorption coefficient of one element, $\mu_{(Zi)}$, depends on the total atomic absorption cross-section (σ_i) of the element for the energy j (Henke et al. 1993). (e, ρ_{diam}), (l, ρ_{air}), and (h, ρ_{fluid}) are respectively the thickness (cm) and the mass density ρ (g/cm^3) of diamonds, air, and fluid. The mass density of the fluid (ρ_{fluid}) changes as the pressure and temperature conditions of the experiment change. β corresponds to the angle between the transmitted incident beam (E_0) and the position of the detector. X represents the path length of the incident beam through the sample, which will excite the fluorescence of a fluid layer of thickness dX. Ω and $\varepsilon(E_x)$ are the subtended solid angle of the detector (1.4×10^{-2} steradians) and their efficiency for X-ray photons of E_x energy. The term $\sigma_F(E_0,Z_i)$ is the fluorescence cross-section of the element Zi at 18 keV (σ_{Rb} = 38.71 cm^2/g and σ_{Sr} = 42.68 cm^2/g), which includes the K partial photoionization cross-section, the fluorescence yield ϖ_K, and the branching ratio $\upsilon_K\alpha/\upsilon_K\beta$ (Sparks 1980). Finally, C_i is the concentration (g_{Zi}/g_{sample}) of element Zi in the sample.

Integrating Equation 1 along the sample thickness leads to the expression:

$$N(E_X,Z_i) = N_0 t \frac{\Omega}{4\pi}\varepsilon(E_X)\exp\left[-\left(\mu_{E_0}^{\text{diam}} + \frac{\mu_{E_X}^{\text{diam}}}{\cos\beta}\right)e\rho_{\text{diam}}\right]\exp\left[-\frac{\mu_{E_X}^{\text{air}}\rho_{\text{air}}l}{\cos\beta}\right]$$
$$C_i\sigma_F(E_0,Z_i)\left[\frac{1-\exp\left[-\left(\mu_{E_0}^{\text{fluid}} + \frac{\mu_{E_X}^{\text{fluid}}}{\cos\beta}\right)\rho_{\text{fluid}}h\right]}{\left(\mu_{E_0}^{\text{fluid}} + \frac{\mu_{E_X}^{\text{fluid}}}{\cos\beta}\right)}\right] \quad (3)$$

Assuming that absorption by a 60 μm thin aqueous fluid layer is negligible compared to that of both diamonds (i.e., $\mu_j^{\text{fluid}} << 1$), we can approximate:

$$1-\exp\left[-\left(\mu_{E_0}^{\text{fluid}} + \frac{\mu_{E_X}^{\text{fluid}}}{\cos\beta}\right)\right] \sim \left(\mu_{E_0}^{\text{fluid}} + \frac{\mu_{E_X}^{\text{fluid}}}{\cos\beta}\right)$$

and Equation 3 reduces to:

$$N(E_X,Z_i) = N_0 t \frac{\Omega}{4\pi}\varepsilon(E_X)\exp\left[-\left(\mu_{E_0}^{\text{diam}} + \frac{\mu_{E_X}^{\text{diam}}}{\cos\beta}\right)e\rho_{\text{diam}}\right]$$
$$\exp\left[-\frac{\mu_{E_X}^{\text{air}}\rho_{\text{air}}l}{\cos\beta}\right]C_i\sigma_F(E_0,Z_i)\rho_{\text{fluid}}h \quad (4)$$

From Equation 3, the concentration of element Z_i in the sample (in g_{Zi}/g_{sample}) can be obtained from $N(E_X, Z_i)$, the area under the measured X-ray peak. Values of μ_j^a are calculated from the X-ray oriented program (XOP) package developed at ESRF (Sanchez del Rio and Dejus 1997) and $\sigma_F(E_0,Z_i)$ deduced from tables (Krause et al. 1978). Ratioing the expression for Sr and Rb gives:

$$\frac{N(E_X,\mathrm{Sr})}{N(E_X,\mathrm{Rb})}=\frac{\varepsilon_{(E_{X=14.2\,\mathrm{keV}})}\exp\left[-\left(\frac{\mu^{\mathrm{diam}}_{E_X}}{\cos\beta}\right)e\rho_{\mathrm{diam}}\right]\exp\left[-\left(\frac{\mu^{\mathrm{air}}_{E_X}}{\cos\beta}\right)l\rho_{\mathrm{air}}\right]C_{\mathrm{Sr}}\sigma_{F(E_0,\mathrm{Sr})}}{\varepsilon_{(E_{X=13.4\,\mathrm{keV}})}\exp\left[-\left(\frac{\mu^{\mathrm{diam}}_{E_X}}{\cos\beta}\right)e\rho_{\mathrm{diam}}\right]\exp\left[-\left(\frac{\mu^{\mathrm{air}}_{E_X}}{\cos\beta}\right)l\rho_{\mathrm{air}}\right]C_{\mathrm{Rb}}\sigma_{F(E_0,\mathrm{Rb})}} \quad (5)$$

Because the Si(Li) detector shows unity intrinsic efficiencies for X-ray energies ranging from 8 to 30 keV (Jaklevic and Giauque 1993), and differences in the absorption for Sr and Rb K_α lines in air and diamond are negligible, the Sr concentration in the fluid can be deduced from the following equation:

$$\left(\frac{C_{\mathrm{Sr}}}{C_{\mathrm{Rb}}}\right)=\frac{N(E_X,\mathrm{Sr})}{N(E_X,\mathrm{Rb})}\frac{\sigma_F(E_0,\mathrm{Rb})}{\sigma_F(E_0,\mathrm{Sr})} \quad (6)$$

RESULTS

Fluorescence calibration and detection limits

Figure 3 displays the spectrum recorded, at the highest dilution, in a Sr-Rb = 0.001 *m* aqueous solution at 298 K and 0.10(5) GPa, loaded in the DAC. The exposure time for the measurements was 300 seconds. The technique, however, did not reach its lowest detection limit, which can be calculated from the spectrum in Figure 3 using the formalism described by Helsen and Kuczumow (1993). Therefore, the minimum detection limit (MDL) using a 15° collection geometry is about 6 ppm ($\sim 6\times10^{-5}\,m$) for Sr and Rb in a fluid placed between the diamond windows of a standard DAC.

The inset in Figure 4 illustrates the spectra collected for the standard solution with Sr = 0.08 *m* and Rb = 0.02 *m* at 298 K and 0.10(5) GPa in the cell. The fluorescence calibration of these elements was obtained from the known concentration ratio of the standard solutions plotted against the measured peak area ratios, as shown in the Figure 4. The slope of the linear relation obtained from the figure is equal, within error, to the ratio of the fluorescence cross-sections at 18 keV: $s_F(E_0,\mathrm{Rb})/s_F(E_0,\mathrm{Sr})$ = 0.907(45), showing that the assumptions developed above to obtain Equation 6 are realistic. This coefficient is slightly smaller than 1 because the Sr*K*-edge at 16.1 keV is closer to the 18 keV exciting incident energy than the Rb *K*-edge at 15.2 keV. Hence, the Sr^{2+} concentration in the fluid can be derived simply from the measured peak area ratios within the approximation described in Equation 6, using the value obtained from the calibration as a correction factor (Fig. 4).

High pressure-high temperature dissolution of $SrCO_3$

Dissolution of strontianite in H_2O was measured in two runs as a function of pressure (up to 3.6 GPa), along isothermal paths. The pressure and temperature changes that occurred in each run are given in Figure 5, together with the evolution of the Sr^{2+} concentration in the fluid. It should be noted that, along all investigated isotherms, $SrCO_3$ dissolution strongly increases as a function of pressure, extending at high pressure the early low pressure observations (Helz and Holland 1965).

Images of the experimental charge in the compression chamber taken at the beginning and the end of the second run are displayed in Figure 6. These images were taken by the X-ray CCD camera in the course of the alignment procedure. They show that the $SrCO_3$ crystal decreased in size during the run, as

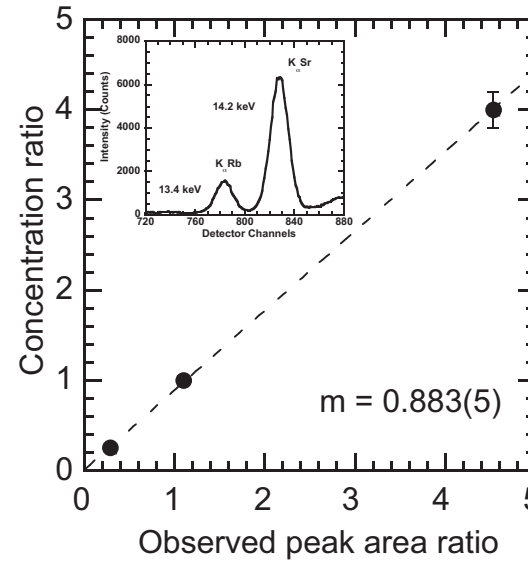

FIGURE 4. Plot of the known Sr/Rb concentration ratios vs. observed peak area ratio for the three standard solutions used in fluorescence calibration. The dashed line, with a slope of 0.883(5), represents the best fit to the data. Inset = SXRF spectrum collected for the standard solution (Sr = 0.08 *m*, Rb = 0.02 *m*) at 298 K and 0.1 GPa in the DAC.

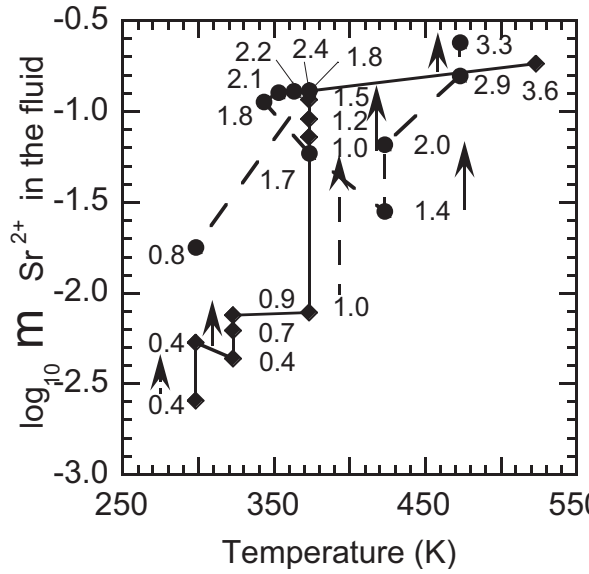

FIGURE 5. Evolution of Sr^{2+} (aq) concentration in the fluid as a function of *P-T* conditions investigated during the experimental runs. The symbol sizes exceed the standard deviation estimated for concentrations. Values correspond to pressure in GPa. Dashed and solid lines indicate the *P-T* path follow during the first and second run respectively. Vertical solid arrows show pressure effects on Sr^{2+} concentration at a given *T*. Vertical dashed arrows represent kinetic effects at given *P-T* conditions.

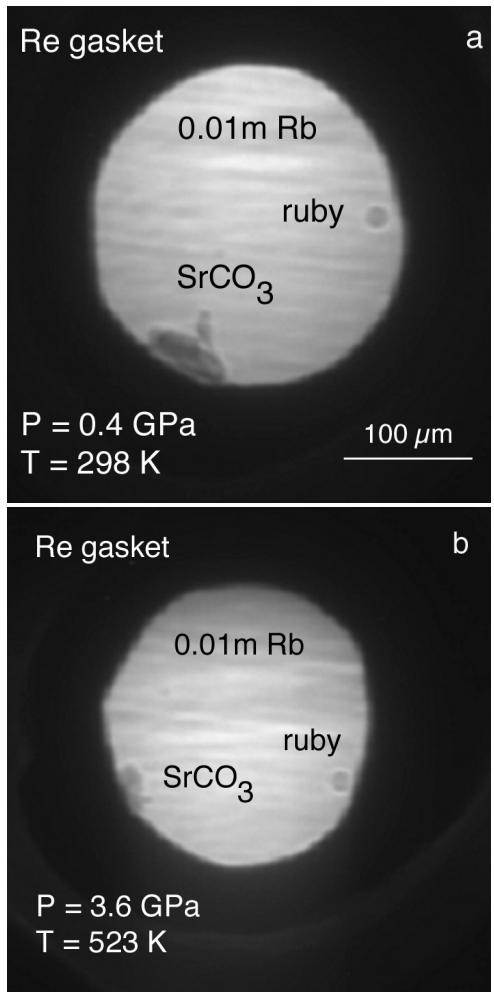

FIGURE 6. X-ray images of a $SrCO_3$ sample together with a ruby chip in the compression chamber at the beginning (**a**) and the end (**b**) of the second experimental run. Note the decrease in size of the $SrCO_3$ crystal during the run.

temperature and pressure were finally increased to 523 K and 3.6 GPa at the end of the run.

The dissolution of strontianite is also evidenced by the large changes in the intensity of the Sr fluorescence peak observed in the fluid, as shown by the spectra recorded at 0.4 GPa, 298 K and 3.6 GPa, 523 K (Fig. 7). This intensity change is associated with an increase in Sr^{2+}(aq) concentration in the fluid from about 0.002 *m* at initial conditions to about 0.18 *m* at the end of the run.

Kinetic effects may be important for the increase in Sr^{2+} concentrations observed between 323 and 373 K, as there is almost no pressure change (0.9 to 1 GPa). We actually tested these kinetic effects by repeatedly analyzing the fluid, leaving the strontianite crystal to react up to 3000 seconds at the same *P-T* conditions. The results are presented in Figure 8 and show that Sr^{2+} concentration in the fluid still increases after 3000 seconds under high-pressure, high-temperature conditions, suggesting that equilibrium has not yet been reached. The measured dissolution values are thus the result of an interplay between thermodynamic and kinetic parameters.

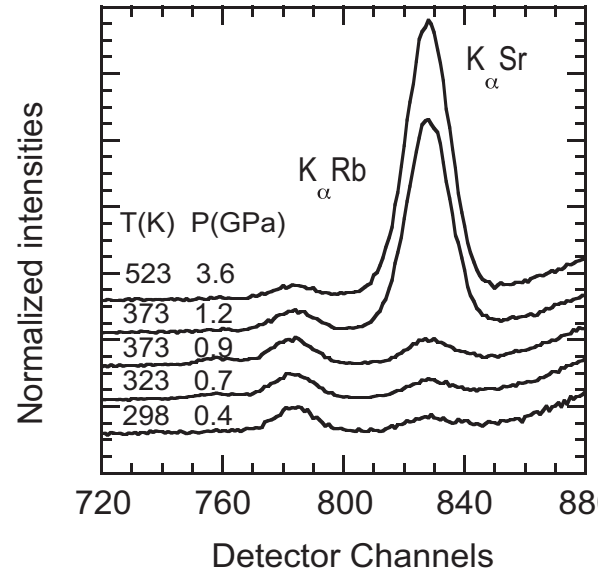

FIGURE 7. SXRF spectra collected in the fluid during dissolution measurements at different *P-T* conditions. The spectra are offset along the intensity axis for clarity.

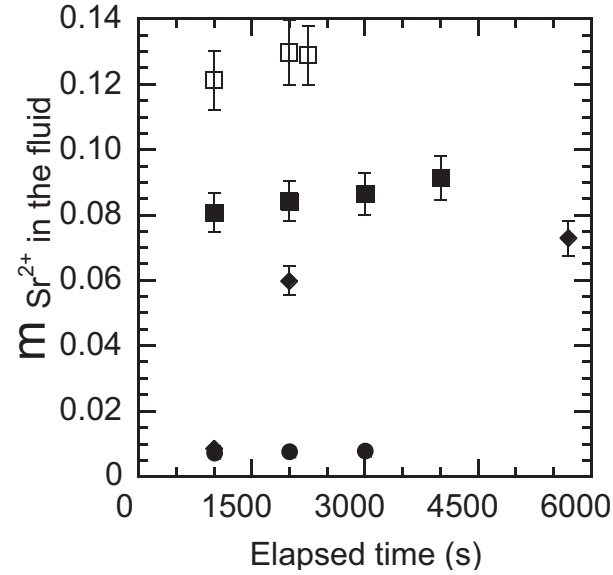

FIGURE 8. Time dependence of the Sr^{2+} concentration in the fluid at various *P-T* conditions. (filled circles = 323 K, 0.9 GPa; diamonds = 323 K, 1.0 GPa; filled squares = 373 K, 1.2 GPa; open squares = 373 K, 1.8 GPa). Error bars are estimated to be 8% of the calculated concentration values. The symbols size exceeds the standard deviation estimated for concentration data at 323 K and 0.9 GPa. The reaction rates are compatible with a first-order law.

DISCUSSION

Figure 3 demonstrates that detection of Sr and Rb in a fluid loaded in the DAC can be performed quantitatively in a transmission geometry at least down to the 1000 ppm concentration level. From this figure, the minimum detection limit (MDL) using a 15° collection geometry has been calculated to be about

6 ppm (~6×10^{-5} *m*) for Sr and Rb in a fluid placed in a DAC. However, these concentration values are much higher than those detected with the generally used 90° geometry (Philippot et al. 1998; Ménez et al. 2001; Ménez et al. 2002). For an equivalent time of measurement (1000 s), the MDL is approximately 200 ppb for Rb and Sr. The reasons for these differences are: (1) the highly absorbent environment of the sample (diamond anvils), which decreases the fluorescence, and (2) the large Compton/Rayleigh scattering in the 15° geometry of our experiment, which constitutes the largest contribution to the background, and thus decreases the sensitivity of the measurements. This background can be reduced substantially when the detector is located at a right angle to the incident beam, in the plane of the storage ring. This experimental configuration would require changes in the original design of the DAC, i.e., a groove cut into the culet of one diamond anvil would reduce the pathway of the fluorescence X-rays, minimizing their attenuation and allowing the collection in the standard horizontal 90° orientation to the incident X-ray beam (Schmidt and Rickers 2002). However, this design significantly reduces the pressure limits of the SXRF analysis, as the strength of the cut diamond is drastically lowered.

If equilibrium were reached, the measured Sr^{2+}(aq) concentration in the experiment would lead to the determination of the solubility of $SrCO_3$ at high pressure and temperature. Due to kinetic hindrances, the measured Sr molalities are, in most cases, lower than the actual solubility at a given pressure and temperature, because we followed a *P-T* path for which the solubility should increase. We will thus consider our data as minimum values for the high *P-T* solubility; the main points discussed below are thus valid even though thermodynamic equilibrium has not been completed. Further studies are needed to establish the kinetic laws associated with this dissolution reaction and to determine solubility values at thermodynamic equilibrium.

Pressure effects on $SrCO_3$ dissolution are noticeable. There is a strong increase in the Sr^{2+} concentration measured in the fluid between 1 bar and 2 GPa. This tendency has been observed up to the highest pressures and temperatures investigated, as shown in Figure 5. Such concentration changes indicates that $SrCO_3$ solubility has increased by at least two orders of magnitude in the overall pressure and temperature range explored.

The effects of temperature on strontianite solubility cannot be derived simply from the present measurements, as data were recorded along isotherms. Due to changes in the mechanical properties of the cell with temperature, it is difficult to perform isobaric runs in a DAC. In fact, when temperature is increased, the expansion of the He gas that drives the membrane of the cell increases the pressure. For instance, decreasing the temperature from 373 to 343 K (Fig. 5) should increase the measured Sr^{2+} concentration in the fluid (Helz and Holland 1965; Busenberg et al. 1984). But this effect is by far counterbalanced by the simultaneous decrease in pressure (2.4 to 1.8 GPa), which causes a large decrease in the Sr^{2+} concentration measured.

The large dissolution, and thus very likely the large solubility of strontianite with increasing pressure at constant temperature, can be understood qualitatively considering the large negative standard reaction volume (ΔV = –58.9 cm^3/mol) of the dissolution reaction:

$$SrCO_3\,(s) \leftrightarrow Sr^{2+}\,(aq) + CO_3^{2-}\,(aq) \qquad (7)$$

Implicit in this qualitative argument is the approximation that pressure effects on acidity constants in the hydrogenocarbonate/carbonate system and on pH are smaller than those on the solubility product, a likely hypothesis when the large ΔV of reaction 7 is considered. Another approximation is that non-ideal parameters will not counteract this effect, which could be the case if Sr species other than Sr^{2+}(aq) were present at high levels in the solutions. Further speciation studies are needed to clarify this issue. Nevertheless, such a solubility increase has already been observed at low pressures (Helz and Holland 1965), but a lack of thermodynamic data on aqueous species prevented those authors from extrapolating their results to pressures as high as those investigated in the present study.

The results of the high-pressure, high-temperature kinetic study reported in Figure 8 suggests that the reaction rates are essentially compatible with a first-order law, as observed previously by Sonderegger et al. (1976) up to 50 °C. Nevertheless, we do not have enough data to establish a kinetic law that describes the temporal evolution of the dissolution reaction.

The present study thus emphasizes that SXRF is a suitable technique for in-situ monitoring of elemental fluorescence in a fluid during dissolution of minerals at high *P-T* conditions in a standard DAC. This technique can be applied to elements with $Z > 28$, for which the characteristic X-ray fluorescence lines emitted are highly transmitted by 2 mm thick diamond anvil. The possibility of collecting in-situ concentration data as a function of time is of great value because knowledge of dissolution rates of minerals could lead to a better understanding of dissolution mechanisms.

The above experimental results have nevertheless important consequences for quantitative modelling of Sr behavior in subduction zones because they show that the solubility of strontianite in pure H_2O is increased at least two fold between 0.4 GPa and 3.6 GPa. More generally, the results will help to constrain better the thermodynamical modelling of aqueous species at extreme pressures and temperatures.

ACKNOWLEGMENTS

The authors thank C. Douchet and Ph. Telouk (UMR5570 ENSLyon) for carrying out the ICP-MS and ICP-AES analysis of the strontianite sample and Pier-Paolo Zuddas (IPG, Paris) for analyses of the starting solutions. Fruitful discussions with B. Reynard during the course of this work have improved this manuscript.

REFERENCES CITED

Aranovich, L.Y. and Newton, R.C. (1999) Experimental determination of CO_2-H_2O activity-composition relations at 600–1000 °C and 6–14 kbar by reversed decarbonation and dehydration reactions. American Mineralogist, 84, 1319–1332.

Ayers, J.C., and Eggler, D.H. (1995) Partitioning of elements between silicate melts and H_2O-NaCl fluids at 1.5 and 2.0 GPa pressure: implications for mantle metasomatism. Geochimica et Cosmochimica Acta, 59, 4237–4246.

Ayers, J.C., Dittmer, S.K., and Layne, G.D. (1997) Partitioning of elements between peridotite and H_2O at 2.0-3.0 GPa and 900–1100 °C, and application to models of subduction zone process. Earth and Planetary Science Letters, 150, 381–389.

Brenan, J.M., Shaw, H.F., Ryerson, F.J., and Phynney, D.L. (1995). Mineral-aqueous fluid partitioning of trace elements at 900 °C and 2.0 GPa: constraints on the trace elements chemistry of mantle and deep crustal fluids. Geochimica et

Cosmochimica Acta, 59, 3331–3350.
Busenberg, E., Plummer, L.N., and Parker, V.B. (1984) The solubility of strontianite ($SrCO_3$) in CO_2-H_2O solutions between 2 and 91 °C, the associations constants of $SrHCO_3^+$(aq) and $SrCO_3^0$(aq) between 5 and 80 °C, and an evaluation of the thermodynamic properties of Sr^{2+}(aq) and $SrCO_3$(cr) at 25 °C and 1 atm total pressure. Geochimica et Cosmochimica Acta, 48, 2021–2035.
Chervin, J.C., Canny, B., Besson, J.M., and Pruzan, P. (1995) A diamond anvil cell for IR microspectroscopy. Review of Scientific Instruments, 66, 2595–2598.
Fein, J.B. and Walther, J.V. (1987) Calcite solubility in supercritical CO_2-H_2O fluids. Geochimica et Cosmochimica Acta, 51, 1665–1673.
Frantz, J.D., Mao, H.K., Zhang, Y.G., Wu, Y., Thompson, A.C., Underwood, J.H., Giauque, R.D., Jones, K.W., and Rivers, M.L. (1988) Analysis of fluid inclusions by X-ray fluorescence using synchrotron radiation. Chemical Geology, 69, 235–244.
Haehnel, O. (1924) Solubilities and properties of the carbonates of Strontium, Barium and heavy metals in water containing carbon dioxide. Journal für Praktische Chemie, 108, 187–193.
Hawkesworth, C.J., Gallagher, K., Hergt, J.M., and McDemott, F. (1993) Mantle and slab contributions in arc magmas. Annual Reviews of Earth and Planetary Sciences, 21, 175–204.
Helz, G.R. and Holland, H.D. (1965) The solubility and geologic occurrence of Strontianite. Geochimica et Cosmochimica Acta, 29, 1303–1315.
Henke, B.L., Gullikson, E.M., and Davis, J.C. (1993) Atomic Data and Nuclear Data Tables, 54, no. 2, 181–342.
Jaklevic, J.M. and Giauque, R.D. (1993) Semiconductor detectors for X-ray spectrometry. In R.E. van Grieken and A.A. Markowicz, Ed., Handbook of X-ray Spectrometry, vol. 14, p. 152–168. Practical Spectroscopy Series, Marcel Dekker, Inc., New York.
Keppler, H. (1996) Constraints from partitioning experiments on the composition of subduction-zone fluids. Nature, 380, 237–240.
Krause, M.O., Nestor Jr, C.W., Sparks Jr., C.J., and Ricci, E. (1978) ORNL Report Nr. 5399.
Lengeler, B., Schroer, C., Tümmler, J., Benner, B., Richwin, M., Snigirev, A., and Snigireva, I. (1999) Imaging by parabolic refractive lenses in the hard x-ray range. Journal of Synchrotron Radiation, 6, 1153–1167.
Manning, C.E. (1994) The solubility of quartz in H_2O in the lower crust and upper mantle. Geochimica et Cosmochimica Acta, 58, 4381–4839.
Manning, C.E. and Boettcher,S.L. (1994) Rapid-quench hydrothermal experiments at mantle pressures and temperatures. American Mineralogist, 79, 1153–1158.
Mao, H.K., Bell, P.M., Shaner, J.W., and Steinber, D.J. (1978) Specific volume measurements of Cu, Mo, Pd and Ag and calibration of the ruby R_1 fluorescence gauge from 0.06 to 1 Mbar. Journal of Applied Physics, 49, 3276–3283.
Mavrogenes, J.A., Bodnar, R.J., Anderson, A.J., Bajt, S., Sutton, S.R., and Rivers, M.L. (1995) Assessment of the uncertainities and limitations of quantitative elemental analysis of individual fluid inclusions using synchrotron X-ray fluorescence (SXRF). Geochimica et Cosmochimica Acta, 59, 3987–3995.
McCoy, H.N. and Smith, H.J. (1911) Equilibrium between alkali-earth carbonates, Carbon dioxide and water. Journal of the American Chemical Society, 33, 468–473.
McCulloch, M.T. and Gamble, J.A. (1991) Geochemical and geodynamical constraints on subduction zone magmatism. Earth and Planetary Science Letters, 102, 358–374.
Melzer, S. and Wunder, B. (2001) K-Rb-Cs partitioning between phlogopite and fluid: experiments and consequences for the LILE signatures of island arc basalts. Lithos, 59, 69–90.
Ménez, B., Simionovici, A., Philippot, P., Bohic, S., Gibert, F., and Chukalina, M. (2001) X-ray fluorescence micro-tomography of an individual fluid inclusion using a third generation synchrotron light source. Nuclear Instruments and Methods in Physics Research B, 181, 749–754.
Ménez, B., Philippot, P., Bonnin-Mosbah, M., Simionovici, A., and Gibert, F. (2002) Analysis of individual fluid inclusions using Synchrotron X-Ray Fluorescence microprobe: progress toward calibration for trace elements. Geochimica et Cosmochimica Acta, 66, 561–576.
Millero, F.J., Milne, P.J., and Thurmond, V. (1984) The solubility of calcite, strontianite and witherite in NaCl solutions at 25 °C. Geochimica et Cosmochimica Acta, 48, 1141–1143.
Newton, R.C. and Manning, C.E. (2000a) Quartz solubility in concentrated aqueous NaCl solutions at deep crustal-upper mantle pressures and temperatures: 2–15 kbar and 500–900 °C. Geochimica et Cosmochimica Acta, 64, 2993–3005.
———(2000b) Metasomatic phase relations in the system CaO-MgO-SiO_2-H_2O-NaCl at high pressures and temperatures. International Geology Review, 42, 152–162.
Peacock, S.M. (1990) Fluid processes in subduction zones. Science, 248, 329–337.
Philippot, P., Ménez, B., Chevallier, P., Gibert, F., Legrand, F., and Populus, P. (1998) Absorption correction procedures for quantitative analysis of fluid inclusions using synchrotron radiation X-ray fluorescence. Chemical Geology, 144, 121–136.
Plummer, L.N. and Busenberg, E. (1982) The solubilities of calcite, aragonite and vaterite in CO_2-H_2O solutions between 0 and 90 °C, and an evaluation of the aqueous model for the system $CaCO_3$-CO_2-H_2O. Geochimica et Cosmochimica Acta, 46, 1011–1040.
———(1987) Thermodynamics of aragonite-strontianite solid solutions: Results from stoichiometric solubility at 25 and 76 °C. Geochimica et Cosmochimica Acta, 54, 1393–1411.
Ragan, D.R., Gustacsen, R., and Schiferl, D. (1992) Calibration of the R_1 and R_2 fluorescence shift as a function of temperature from 0 to 600 K. Journal of Applied Physics, 72, 5539–5544.
Roedder, E. (1984) Fluid inclusions, vol. 12. Reviews in Mineralogy, Mineralogical Society of America, Washington, D.C.
Sanchez del Rio, M. and Dejus, R.J. (1997) Proccedings SPIE, 3152, 148.
Scambelluri, M. and Philippot, P. (2001) Deep fluids in subduction zones. Lithos, 55, 213–227.
Schmidt, C. and Rickers, K. (2002) *In situ* determination of mineral solubilities at high pressures and temperatures using synchrotron radiation XRF. Hydrothermal fluid geochemistry, EMPG IX, Abstracts, p. 96.
Sharp, W.E. and Kennedy, G.C. (1965) The system CaO-CO_2-H_2O in the two phases region calcite and aqueous solution. Journal of Geology, 73, 391–403.
Snigirev, A., Kohn, V.G., Snigireva, I., and Lengeler, B. (1996) A compound refractive lens for focusing high energy X-rays. Nature, 384, 49–51.
Sonderegger, J.L., Brower, K.R., and LeFebre, V.G.A. (1976) A preliminary investigation of strontianite dissolution kinetics. American Journal of Science, 276, 997–1022.
Sparks, C.J. (1980) X-ray Fluorescence Microprobe for Chemical Analysis. In H. Winick and S. Doniach, Ed., Synchrotron Radiation Research, p. 459–512. Plenum, New York.
Stalder, R., Foley, S.F., Brey, G.P., and Horn, I. (1998) Mineral-aqueous fluid partitioning of trace elements at 900–1200 °C and 3.0–5.7 GPa: New experimental data for garnet, clinopyroxene, and rutile, and implications for mantle metasomatism. Geochimica et Cosmochimica Acta, 62, 1781–1801.
Vekemans, B., Janssens, K., Vincze, L., Adams, F., and Van Espen, P. (1994) Analysis of X-ray spectra by iterative least squares (AXIL): New developments. X-Ray Spectrometry, 23, 278–285.
Walther, J.V. and Orville, P.M. (1983) The extraction-quench technique for determination of the thermodynamic properties of solute complex: application to quartz solubility in fluid mixtures. American Mineralogist, 68, 731–741.
Zotov, N. and Keppler, H. (2002) Silica speciation in aqueous fluids at high pressures and high temperatures. Chemical Geology, 184, 71–82.

MANUSCRIPT RECEIVED JULY 18, 2002
MANUSCRIPT ACCEPTED FEBRUARY 3, 2003
MANUSCRIPT HANDLED BY THOMAS DUFFY